Fluorescence correlation spectroscopy with a total internal reflection fluorescence STED microscope (TIRF-STED-FCS)

Marcel Leutenegger,[1] Christian Ringemann,[1] Theo Lasser,[2] Stefan W. Hell,[1] and Christian Eggeling[1,*]

[1] *Department of NanoBiophotonics, Max Planck Institute for Biophysical Chemistry, Am Fassberg 11, 37077 Göttingen, Germany*
[2] *Laboratoire d'Optique Biomédicale, École Polytechnique Fédérale de Lausanne, 1015 Lausanne, Switzerland*
[*] ceggeli@gwdg.de

We characterize a novel fluorescence microscope which combines the high spatial discrimination of a total internal reflection epi-fluorescence (epi-TIRF) microscope with that of stimulated emission depletion (STED) nanoscopy. This combination of high axial confinement and dynamic-active lateral spatial discrimination of the detected fluorescence emission promises imaging and spectroscopy of the structure and function of cell membranes at the macro-molecular scale. Following a full theoretical description of the sampling volume and the recording of images of fluorescent beads, we exemplify the performance and limitations of the TIRF-STED nanoscope with particular attention to the polarization state of the laser excitation light. We demonstrate fluorescence correlation spectroscopy (FCS) with the TIRF-STED nanoscope by observing the diffusion of dye molecules in aqueous solutions and of fluorescent lipid analogs in supported lipid bilayers in the presence of background signal. The nanoscope reduced the out-of-focus background signal. A lateral resolution down to 40–50 nm was attained which was ultimately limited by the low lateral signal-to-background ratio inherent to the confocal epi-TIRF scheme. Together with the estimated axial confinement of about 55 nm, our TIRF-STED nanoscope achieved an almost isotropic and less than 1 attoliter small all-optically induced measurement volume.

OCIS codes: (050.1940) Diffraction; (180.2520) Fluorescence microscopy; (260.2510) Fluorescence.

References and links

1. J. B. Pawley, *Handbook of biological confocal microscopy,* 3rd ed., ISBN 0-387-25921-x, Springer, New York (2005).
2. E. Abbe, "Beiträge zur Theorie des Mikroskops und der mikroskopischen Wahrnehmung," Archiv für Mikroskopische Anatomie **9,** 413–468 (1873).
3. S. W. Hell and J. Wichmann, "Breaking the diffraction resolution limit by stimulated emission: stimulated-emission-depletion fluorescence microscopy," Opt. Lett. **19,** 780–782 (1994).
4. T. A. Klar, S. Jakobs, M. Dyba, A. Egner, and S. W. Hell, "Fluorescence microscopy with diffraction resolution limit broken by stimulated emission," Proc. Natl. Ac. Sci. **97,** 8206–8210 (2000).
5. Stefan W. Hell, "Far-field optical nanoscopy," Science **316,** 1153–1158 (2007).
6. V. Westphal and S. W. Hell, "Nanoscale resolution in the focal plane of an optical microscope," Phys. Rev. Lett. **94,** 143903 (2005).
7. B. Harke, C. Ullal, J. Keller, and S. W. Hell, "Three-dimensional nanoscopy of colloidal crystals," Nano Lett. **8,** 1309–1313 (2008).
8. D. Wildanger, R. Medda, L. Kastrup, and S. W. Hell, "A compact STED microscope providing 3D nanoscale resolution," J. Microsc. **236,** 35–43 (2009).
9. R. Schmidt, C. A. Wurm, S. Jakobs, J. Engelhardt, A. Egner, and S. W. Hell, "Spherical nanosized focal spot unravels the interior of cells," Nat. Methods **5,** 539–544 (2008).
10. D. Magde, W. W. Webb, and E. Elson, "Thermodynamic fluctuations in a reacting system - measurement by fluorescence correlation spectroscopy," Phys. Rev. Lett. **29,** 705 (1972).

#158306 - $15.00 USD Received 16 Nov 2011; revised 9 Feb 2012; accepted 10 Feb 2012; published 17 Feb 2012

11. M. Ehrenberg and R. Rigler, "Fluorescence correlation spectroscopy applied to rotational diffusion of macromolecules," Quart. Rev. Biophys. **9,** 69–81 (1976).
12. C. Eggeling, C. Ringemann, R. Medda, G. Schwarzmann, K. Sandhoff, S. Polyakova, V. N. Belov, B. Hein, C. von Middendorff, A. Schönle, and S. W. Hell, "Direct observation of the nanoscale dynamics of membrane lipids in a living cell," Nature **457,** 1159–1163 (2009).
13. L. Kastrup, H. Blom, C. Eggeling, and S. W. Hell, "Fluorescence fluctuation spectroscopy in subdiffraction focal volumes," Phys. Rev. Lett. **94**, 178104 (2005).
14. C. Ringemann, B. Harke, C. von Middendorff, R. Medda, A. Honigmann, R. Wagner, M. Leutenegger, A. Schönle, S. W. Hell, and C. Eggeling, "Exploring single-molecule dynamics with fluorescence nanoscopy," N. J. Phys. **11,** 103054 (2009).
15. D. Axelrod, "Cell-substrate contacts illuminated by total internal reflection fluorescence," J. Cell Biol. **89,** 141–145 (1981).
16. G. A. Truskey, J. S. Burmeister, E. Grapa, and W. M. Reichert, "Total internal reflection fluorescence microscopy (TIRFM). II. Topographical mapping of relative cell/substratum separation distances," J. Cell Sci. **103,** 491–499 (1992).
17. M. Tokunaga, K. Kitamura, K. Saito, A. H. Iwane, and T. Yanagida, "Single molecule imaging of fluorophores and enzymatic reactions achieved by objective-type total internal reflection fluorescence microscopy," Biochem. Biophys. Res. Commun. **235,** 47–53 (1997).
18. A. B. Mathur, G. A. Truskey, and W. M. Reichert, "Atomic force and total internal reflection fluorescence microscopy for the study of force transmission in endothelial cells," Biophys. J. **78,** 1725–1735 (2000).
19. D. Axelrod, "Total internal reflection fluorescence microscopy in cell biology," Traffic **2,** 764–774 (2001).
20. H. Schneckenburger, "Total internal reflection fluorescence microscopy: technical innovations and novel applications," Curr. Opin. Biotechnol. **16,** 13–18 (2005).
21. A. M. Lieto, R. C. Cush, and N. L. Thompson, "Ligand-receptor kinetics measured by total internal reflection with fluorescence correlation spectroscopy," Biophys. J. **85,** 3294–3302 (2003).
22. D. Axelrod, E. H. Hellen, and R. M. Fulbright, "Total internal reflection fluorescence" in *Topics in fluorescence spectroscopy*, J. R. Lakowicz (ed.), vol. **3,** 289–343, ISBN 978-0-306-43954-4, Springer (2002).
23. T. Ruckstuhl and D. Verdes, "Supercritical angle fluorescence (SAF) microscopy," Opt. Express **12,** 4246–4254 (2004).
24. N. L. Thompson, T. P. Burghardt, and D. Axelrod, "Measuring surface dynamics of biomolecules by total internal reflection fluorescence with photobleaching recovery or correlation spectroscopy," Biophys. J. **33,** 435–454 (1981).
25. K. Hassler, T. Anhut, R. Rigler, M. Gösch, and T. Lasser, "High count rates with total internal reflection fluorescence correlation spectroscopy," Biophys. J. **88,** L01–L03 (2005).
26. W. T. Welford, "Use of annular apertures to increase focal depth," J. Opt. Soc. Am. A **50,** 749–753 (1960).
27. R. M. Herman and T. A. Wiggins, "Production and uses of diffractionless beams," J. Opt. Soc. Am. A **8,** 932–942 (1991).
28. T. Ruckstuhl and S. Seeger, "Attoliter detection volumes by confocal total-internal-reflection fluorescence microscopy," Opt. Lett. **29,** 569–571 (2004).
29. J. W. M. Chon, M. Gu, C. Bullen, and P. Mulvaney, "Two-photon fluorescence scanning near-field microscopy based on a focused evanescent field under total internal reflection," Opt. Lett. **28,** 1930–1932 (2003).
30. T. J. Gould, J. R. Myers, and J. Bewersdorf, "Total internal reflection STED microscopy," Opt. Express **19,** 13351–13357 (2011).
31. K. I. Willig, J. Keller, M. Bossi, and S. W. Hell, "STED microscopy resolves nanoparticle assemblies," N. J. Phys. **8,** 106 (2006).
32. M. Leutenegger, R. Rao, R. A. Leitgeb, and T. Lasser, "Fast focus field calculations," Opt. Express **14**(23), 11277–11291 (2006).
33. M. Leutenegger and T. Lasser, "Detection efficiency in total internal reflection fluorescence microscopy," Opt. Express **16**(12), 8519–8531 (2008).
34. R. Dorn, S. Quabis, and G. Leuchs, "Sharper focus for a radially polarized light beam," Phys. Rev. Lett. **91,** 233901 (2003).
35. M. Leutenegger, C. Eggeling, and S. W. Hell, "Analytical description of STED microscopy performance," Opt. Express **18**(25), 26418–26430 (2010).
36. W. Lukosz and R. E. Kunz, "Light-emission by magnetic and electric dipoles close to a plane interface: 1. Total radiated power," J. Opt. Soc. Am. **67,** 1607–1615 (1977).
37. G. W. Ford and W. H. Weber, "Electromagnetic interactions of molecules with metal surfaces," Phys. Rep. **113,** 195–287 (1984).
38. A. Honigmann, C. Walter, F. Erdmann, C. Eggeling, and R. Wagner, "Characterization of horizontal lipid bilayers as a model system to study lipid phase separation," Biophys. J. **98,** 2886–2894 (2010).
39. S. Chiantia, N. Kahya, and P. Schwille, "Dehydration damage of domain-exhibiting supported bilayers: an AFM study on the protective effects of disaccharides and other stabilizing substances," Langmuir **21,** 6317–6323 (2005).
40. J. Widengren, U. Mets, and R. Rigler, "Fluorescence correlation spectroscopy of triplet states in solution: A theoretical and experimental study," J. Phys. Chem. **99,** 13368–13379 (1995).
41. S. Chiantia, J. Ries, N. Kahya, and P. Schwille, "Combined AFM and two-focus SFCS study of raft-exhibiting model membranes," ChemPhysChem **7,** 2409–2418 (2006).

#158306 - $15.00 USD Received 16 Nov 2011; revised 9 Feb 2012; accepted 10 Feb 2012; published 17 Feb 2012

42. U. Golebiewska, M. Nyako, W. Woturski, I. Zaitseva, and S. McLaughlin, "Diffusion coefficient of fluorescent phosphatidylinositol 4,5-bisphosphate in the plasma membrane of cells," Mol. Biol. Cell **19,** 1663–1669 (2008).
43. T. Dertinger, V. Pacheco, I. von der Hocht, R. Hartmann, I. Gregor, and J. Enderlein, "Two-focus fluorescence correlation spectroscopy: A new tool for accurate and absolute diffusion measurements," ChemPhysChem **2007**(8), 433–443 (2007).
44. D. E. Koppel, "Statistical accuracy in fluorescence correlation spectroscopy," Phys. Rev. A **10,** 1938–1945 (1974).
45. E. Rittweger, B. R. Rankin, V. Westphal, and S. W. Hell, "Fluorescence depletion mechanisms in super-resolving STED microscopy," Chem. Phys. Lett. **442,** 483–487 (2007).
46. K. Kolmakov, V. N. Belov, J. Bierwagen, C. Ringemann, V. Mueller, C. Eggeling, and S. W. Hell, "Red-emitting rhodamine dyes for fluorescence microscopy and nanoscopy," Chem. Eur. J. **16,** 158–166 (2010).
47. S. W. Hell and E. H. K. Stelzer, "Properties of a 4Pi confocal fluorescence microscope," J. Opt. Soc. Am. A **9,** 2159–2166 (1992).
48. M. Gu and C. J. R. Sheppard, "Three-dimensional transfer functions in 4Pi confocal microscopes," J. Opt. Soc. Am. A **11,** 1619–1627 (1994).
49. K. Hassler, *Single molecule detection and fluorescence correlation spectroscopy on surfaces*, doctoral thesis, École Polytechnique Fédérale de Lausanne, Switzerland (2005): http://library.epfl.ch/theses/?nr=3433.

1. Introduction

The monitoring of biologically relevant structures and reactions down to the single-molecule level with fluorescence tagging has become one of the most promising approaches for understanding a variety of phenomena in biophysics, biochemistry and life science. By applying techniques of fluorescence spectroscopy to labeled biomolecules, a manifold of important parameters become accessible. For example, molecular dynamics, energy transfer, and ligand–receptor reactions can be monitored at the molecular level. This vast application field is a major drive for innovative optical methods because it opens the door for new quantitative insights of molecular interactions on a nanoscopic scale. Since the advent of the confocal laser scanning microscope (LSM), fluorescence microscopy and spectroscopy are often performed on the very same instrument. It offers a small observation volume for spectroscopic measurements together with the ability to quickly image the three-dimensional structures of interest with high spatial resolution and minimal invasion. This combined capability of imaging the structure and measuring spectroscopic properties of interesting features both with high signal-to-background ratio (SBR) and high signal-to-noise ratio (SNR) makes the LSM a workhorse in fluorescence microscopy [1]. However, due to diffraction, its spatial resolution is limited to >200 nm for visible light, meaning that objects of the same kind cannot be resolved on smaller scales [2]. Fortunately, many of the growing demands for diffraction-unlimited far-field imaging and spectroscopy at the molecular scale can be satisfied with stimulated emission depletion (STED) microscopy [3–5]. Whereas it is relatively simple to strongly improve just the lateral [6] or the axial [4] resolution by STED, a large improvement of resolution along all spatial directions requires more complex instrumentation. Two powerful concepts were shown so far. The first concept applies simultaneous irradiation by two STED beams, one improving the lateral and the other one the axial resolution [7,8]. The second concept uses a 4Pi microscope with coherently used opposing lenses to simultaneously improve the resolution in all three dimensions [9]. While these concepts improve the resolution by reducing the measurement volume in the axial direction, many applications require just the axial volume reduction without imaging along the optical axis. This is particularly the case for imaging and spectroscopic investigations that can be carried out on a (glass) surface. Thereafter, if confining the measurement to a surface is acceptable, i.e. far-field wave propagation is given up along the optical axis, one can resort to total internal reflection (TIR) as a means to reduce the axial extent of the measurement volume. Here, we investigate a TIR based approach using evanescent optical fields for fluorophore excitation in order to reduce the axial extent of the measurement volume below 100 nm.

Fluorescence microscopy has reached a sensitivity that allows the detection of single molecules with high temporal resolution. It is thus ideally suited for studying cellular dynamics on the molecular level. The quantitative analysis of such single molecule

#158306 - $15.00 USD Received 16 Nov 2011; revised 9 Feb 2012; accepted 10 Feb 2012; published 17 Feb 2012

experiments is readily performed by studying the fluctuations of the fluorescence signal using well established techniques such as fluorescence correlation spectroscopy (FCS) [10,11]. However, these techniques are also diffraction-limited, and standard confocal microscopy usually averages the details of nanoscale molecular dynamics. Recently, combining FCS with STED [12–14] allowed direct measurements at the length scale of interest. STED-FCS directly revealed nanoscopic details of membrane lipid dynamics that are not observable with diffraction-limited measurement volumes [12]. However, all STED experiments so far have been hampered by the out-of-focus background signal [12–14] demanding further axial reduction of the measurement volume.

In wide-field fluorescence microscopy, the background from out-of-focus structures can be efficiently suppressed by confining the excitation light into a thin layer. This is commonly achieved by an evanescent illumination of the sample by TIR of the excitation light at the cover slip–sample interface [15]. TIR fluorescence microscopy (TIRFM) is receiving much attention, both because of its simple implementation using either lenses of high numerical aperture or prism-based illumination, and its exceptional performance with respect to the contrast of the imaged structures at the interface versus structures in the volume (see for example [16–23]). TIRFM only detects the fluorophores near the cover glass–sample interface because of the finite penetration depth of the evanescent excitation field of typically <100 nm. TIRFM is virtually a two-dimensional microscopy technique, i.e. not a genuine far-field optical technique. Consequently, it is not really applicable to explore the interior of a cell, but rather its boundaries such as the plasma membrane and ligand-receptor interactions (see for example [21,24]). Whereas TIRFM is well suited for wide-field imaging with an illumination extending laterally over several micrometers, it is less so for fluorescence spectroscopy because the evanescent illumination is difficult to confine laterally. Several attempts have been made in the past to overcome this limitation. For instance, Thompson et al. [24] and Hassler et al. [25] used a confocal detection pinhole for the lateral confinement, which resulted in a disc like observation volume. If neither the available excitation power nor the photo-bleaching of a large area is an issue, spectroscopic measurements of, for example, surface-bound molecules can be performed. However, when it comes to detecting fluorophores dwelling close to the interface, as for instance labeled constituents of cell membranes, illuminating a large area should be avoided because photo-bleaching would bleach most fluorophores long before they ever reach the measurement volume. In this case, an annular laser illumination can provide an evanescent excitation confined within a central peak that is surrounded by weakening side lobes (Bessel beam like pattern) [26,27]. Because of the lateral confinement, the annular illumination is also quite power efficient. An average laser power of 100–150 μW in the objective aperture is sufficient for an average excitation intensity of 10 kW/cm^2 in the focus, which qualifies the instrument for fluorescence spectroscopy using pulsed diode lasers. Unfortunately, the intensity in the first side lobe reaches typically 20–30% of the central peak intensity and the induced emission cannot be truncated by the detection pinhole alone [28]. However, it can be reduced by two-photon excitation [29].

In a recent report [30], confocal epi-TIRF was combined with STED. A lateral resolution of 50 nm and an axial confinement to 70 nm was reported, exemplified on images of fluorescent beads and immunolabeled fixed cells. Here, we present a full theoretical description of the sampling volume of TIRF-STED nanoscopy and examine the advantages and limitations of confocal epi-TIRF-STED nanoscopy for imaging and FCS measurements. We find that the polarization of the laser light is critical, as well as the side lobes of the TIR excitation spot. In our approach, the confocal pinhole blocks the emission induced by all side lobes except the first one, from which the emission of the fluorophores is then actively inhibited by STED. By applying a higher STED power than required for the side lobe suppression allowed an increasing of the sharpness of the central peak. As a result, an almost isotropic observation volume of <1 attoliter and <50 nm diameter was achieved and FCS measurements could be performed in areas of <40 nm diameter in the presence of strong out-of-focus background.

#158306 - $15.00 USD Received 16 Nov 2011; revised 9 Feb 2012; accepted 10 Feb 2012; published 17 Feb 2012

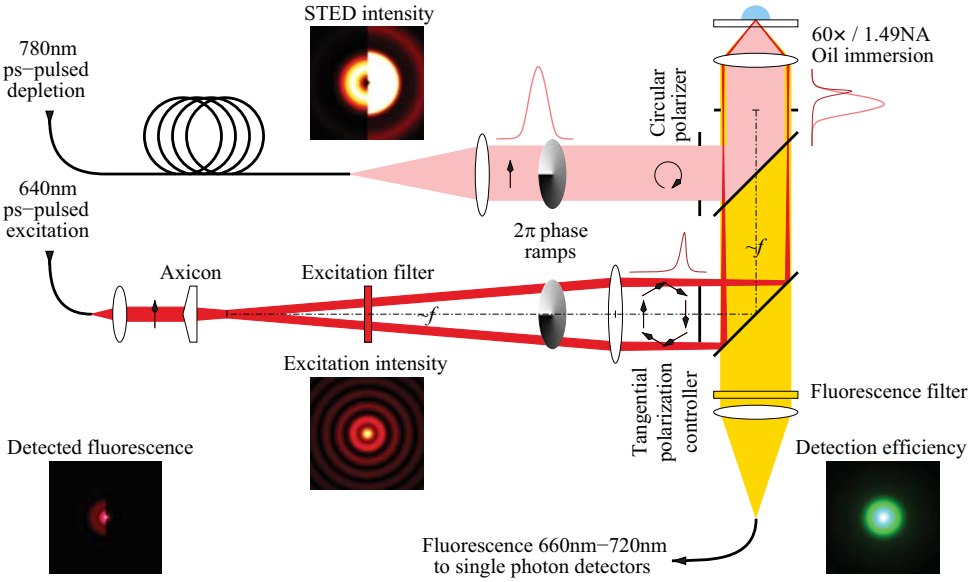

Fig. 1: Confocal epi-TIRF-STED setup. Lenses are indicated by white ellipsoids. The distance *f* indicates the focal length of the tube lens between the phase ramp and the tangential polarization controller. Insets show the calculated lateral two-dimensional profiles (2×2 μm^2) in the plane 5 nm above the cover slip surface of the excitation intensity with tangential polarization, of the STED intensity distribution with circular polarization (left half: laser intensity, right: fluorescence inhibition efficiency at high power), of the detection efficiency and of the brightness of the detected fluorescence (left half: no STED; right: high STED power).

2. TIRF-STED design

Figure 1 outlines the configuration of our confocal epi-TIRF-STED nanoscope. An excitation laser provides picosecond pulses or continuous-wave (CW) light to pump the fluorophores into the excited state. At the high numerical aperture (NA) oil immersion objective aperture, an annular illumination with a nearly flat wavefront is needed to achieve a well-focused excitation intensity spot under total internal reflection. This particular illumination is provided either by an axicon creating a conical wavefront, which is then focused by a lens into the desired ring pattern at the objective lens aperture (as described in this report), or by blocking the central part of the collimated laser beam in front of the objective (as done in [30]), which however discards >90% of the laser power. The polarization controller modifies the linear polarization of the annular beam to tangential polarization, which is of particular importance for achieving a well-confined excitation spot and efficient STED as outlined later. A 2π phase ramp (vortex plate) is inserted to restore the central peak. The STED laser provides pulsed or CW light to inhibit the fluorescence from the excitation volume except at some tiny region at the focal center. A quarter-wave plate and another 2π phase ramp (vortex plate) induce a donut shaped intensity distribution of the STED beam with circular polarization [31]. A diaphragm may be used to inhibit TIR for the STED beam, such that the bright STED beam will not be collected by the TIRF objective. Instead, we used two emission filters for achieving a sufficient blocking ratio. Similar to the excitation, an axicon–lens pair may be used in the STED beam for confining the stimulated emission by an evanescent field as well. Dichroic mirrors and dielectric band pass filters are used to combine the excitation and the STED beams and to separate the fluorescence emission. Finally, the tube lens focuses the fluorescence emission through a confocal pinhole onto a photon counting detector. A detailed description of our present instrument and its key components is listed in the appendix.

#158306 - $15.00 USD Received 16 Nov 2011; revised 9 Feb 2012; accepted 10 Feb 2012; published 17 Feb 2012

For efficient confinement of the sampling volume by the STED beam, the shape and mutual alignment of the excitation and STED foci as well as their polarizations have to match. Due to the laterally extended excitation, the diameter of the confocal pinhole need to be matched in order to efficiently reject the fluorescence from the side lobes of the evanescent excitation focus without compromising the detection efficiency in the central peak. Therefore, we estimated the performance of our confocal epi-TIRF-STED microscope based on the fluorescence excitation and detection framework by Leutenegger et al. [32,33]. The most promising profiles of the excitation and the STED beams as well as their polarizations at the interface are shown in Fig. 2 and Fig. 3, respectively. For the retained optimal configuration, the estimated three-dimensional foci are shown in Fig. 4 and the resulting sampling volumes are shown in Fig. 5.

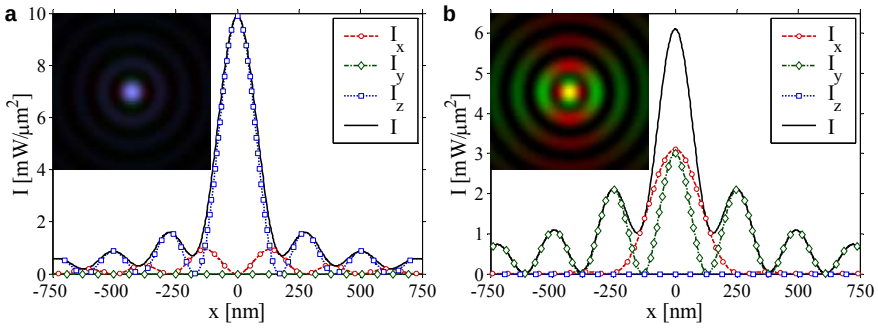

Fig. 2: Evanescent excitation foci for (a) radially and (b) tangentially polarized light. Calculated cross-sections along the lateral x direction of the evanescent excitation profiles created with an annular illumination of the objective aperture, such that only super-critical angles are illuminated. Shown are the total intensity I (black line) and the relative intensities of the lateral x- (red circles) and y- (green circles) and the axial z-polarization (blue squares) components. The wavelength and power of the laser and the refractive index n of the sample were set to λ_{ex} = 640 nm, 1 mW and n = 1.33 (water). The insets show the lateral two-dimensional intensity distributions at the cover slip–sample interface (red: x-, green: y- and blue: z-polarized component). (a) Along the x-axis, the radial polarization leads to an overwhelming z-, a zero y- and a small x-polarized intensity component, which has a central intensity minimum. (b) Tangential polarization results in x- and y-polarized intensity components of similar amplitude and a zero z-polarized component.

2.1. Excitation

Figure 2 compares the calculated evanescent excitation foci along the lateral x direction obtained with the axicon–lens pair and by varying the polarization and phase of the incident excitation beam. It is worth emphasizing that the polarization of the laser beam is decisive for the shape of the central peak. Therefore, besides the total intensity I of the laser profile, Fig. 2 also plots the intensity profiles of the two lateral in-plane polarization components I_x and I_y and the axial polarization component I_z. With a radially polarized beam (a), the excitation focus is confined to a strong central peak of 177 nm full-width-at-half-maximum (FWHM) in diameter, mainly made up by axially polarized light I_z. The lateral polarization components I_x and I_y are weak and have a central intensity minimum. The penetration depth at half-maximum is 72 nm. In case (b), the tangential polarization and the vortex plate lead to a slightly sharper central intensity peak of 166 nm FWHM in diameter at the expense of stronger lobes. The penetration depth at half-maximum is again 72 nm. The polarization in the central peak is rotating around the optical axis as shown by inset (b), but there is no axial polarization component at all. Without the vortex plate, excitation with tangential polarization would produce a central minimum in the evanescent field similar to that of I_x and I_y in case (a). Excitation with linearly polarized light leads to a bow-tie shape of the evanescent focus with 387 nm and 186 nm lateral FWHM and 72 nm penetration depth [28,29] and circularly polarized excitation results in a Mexican hat focus with 322 nm lateral FWHM and 72 nm

#158306 - $15.00 USD Received 16 Nov 2011; revised 9 Feb 2012; accepted 10 Feb 2012; published 17 Feb 2012

penetration depth (data not shown). The smallest focal diameter is thus realized with tangential polarization, however at the expense of large side lobes (see e.g. [34]). The smallest focus in terms of energy concentration is reached with radial polarization, because in this case the side lobes are least pronounced. These weak side lobes seem to suggest the use of radially polarized laser light for TIRF excitation as implemented by Gould et al. [30]. Unfortunately, the resulting excitation field is mainly axially polarized, which can pose challenges in fluorescence experiments.

STED is usually most efficient if the polarization is the same as for the excitation. As we will see in Fig. 3, the effect of the axial polarization component I_z of the excitation field is more difficult to suppress, because the STED focus has almost no z-polarized component close to the central minimum. For rapidly rotating fluorophores, this polarization mismatch will pose no challenge if the average rotation time is much shorter than the fluorescence lifetime and shorter than the STED pulse duration. However, we preferred excitation with tangentially polarized light in order to maximize the STED efficiency for any kind of sample, i.e. also for fixed fluorophores.

2.2 Stimulated emission depletion

Figure 3 outlines two non-evanescent foci of the STED light providing well-defined donut profiles with a central intensity minimum ("zero"). Again, the intensity profiles of the two lateral in-plane polarization components I_x and I_y and the axial polarization component I_z are plotted along with the total intensity I. Circular polarization (a) is the better choice as it strongly suppresses both lateral polarization components, i.e. x- and y-oriented emission dipoles, independent of the fluorophore's position in the focal periphery. The in-plane intensity components I_x and I_y show an almost identical steepness around the zero regardless of the different peak values. The small axial polarization component I_z improves the emission suppression of rotating fluorophores but only within a ring of about 650 nm in diameter. Compared to the circular polarization, the tangential polarization (b) is less efficient as it suppresses exclusively the tangential component of the fluorophores emission dipole.

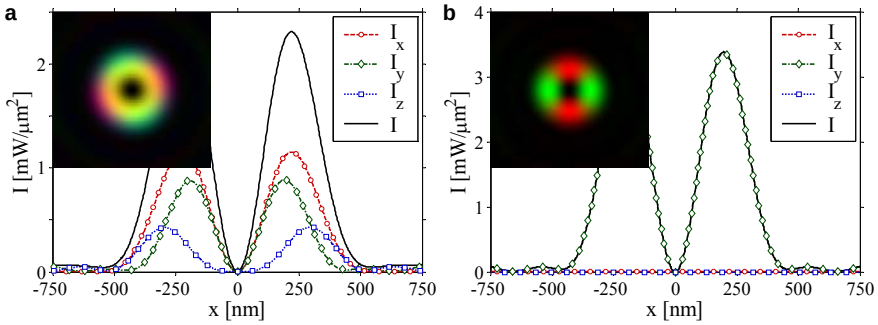

Fig. 3: Donut-shaped non-evanescent STED foci for (a) circular and (b) tangentially polarized light. Calculated cross-sections along the lateral x direction of the non-evanescent intensity profiles of the STED foci created by overfilling the objective aperture 1.7×. Shown are the total intensity I (black line) and the relative intensities of the lateral x- (red circles) and y- (green circles) and the axial z-polarization (blue squares) components. The wavelength and power of the STED laser and the refractive index n of the sample were set to λ_{STED} = 780 nm, 1 mW and n = 1.33 (water). The insets show the intensity distributions at the cover slip–sample interface (red: x-, green: y- and blue: z-polarized component). With tangential polarization, the y-polarized component contributes 100% of the intensity along the x-axis and vice versa, while a z-polarized component is absent.

No evanescent illumination is assumed in Fig. 3. If the penetration depth of the STED beam were axially confined by TIR similar to the excitation beam, the FWHM of the zero would shrink by ~10% (data not shown). However, the peak intensity would be significantly reduced because the power of the STED light would spread over several rings as shown in Fig. 2 for the evanescent excitation beam. In principle, the best performance would be

#158306 - $15.00 USD Received 16 Nov 2011; revised 9 Feb 2012; accepted 10 Feb 2012; published 17 Feb 2012

achieved with an intermediate profile featuring both super- and sub-critical angle illumination, but it would be very challenging to achieve a large annular illumination with the required (vortex-shaped) wavefront because a power efficient axicon–lens combination does not provide a flat wavefront along the radial direction.

From these theoretical considerations, we conclude that the best match between the polarization of the excitation focus and the STED focus is obtained for tangential polarization of the excitation light and circular polarization of the STED light. This combination is expected to maximize the TIRF-STED performance.

2.3 Effective brightness profile

Figure 4 shows the calculated three-dimensional ($\vec{r} = (x, y, z)$) profiles of (a) the excitation intensity $I_{ex}(\vec{r})$ for tangentially polarized light and (b) the STED intensity $I_{STED}(\vec{r})$ for circularly polarized light as well as of (c) the detection efficiency $Q(\vec{r})$. While $I_{ex}(\vec{r})$ and $I_{STED}(\vec{r})$ are just the three-dimensional representations of Fig. 2b and Fig. 3a, $Q(\vec{r})$ includes the point-spread function of the objective lens and the confocal pinhole [32,33]. All three profiles now allow us to calculate the brightness profile $B(\vec{r})$ of the detected fluorescence, i.e. to estimate the confinement of the observation volume of our TIRF-STED nanoscope.

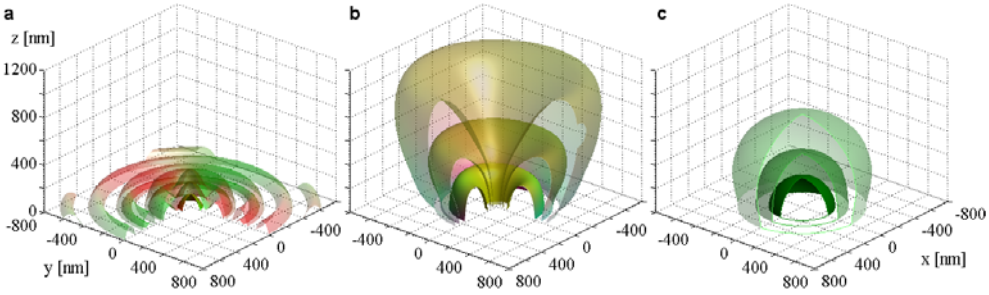

Fig. 4: Calculated e^{-1}, e^{-2} and e^{-3} iso-surfaces of (a) the normalized evanescent excitation intensity I_{ex} (λ_{ex} = 640nm, tangential polarization), (b) the normalized donut-shaped STED intensity I_{STED} (λ_{STED} = 780nm, circular polarization) and of (c) the normalized detection efficiency Q (470nm projected pinhole diameter). The polarization of the laser foci (a,b) is color-coded in red, green and blue representing the x, y and z components, respectively. The refractive index n of the sample was set to 1.33 (water).

The brightness profile $B(\vec{r}) = q_{fl}^{*}(z)k(\vec{r})Q(\vec{r})$ of the detected fluorescence is the product of the local rate of spontaneous decays $k(\vec{r})$ from the excited singlet state (including STED), the local fluorescence quantum yield $q_{fl}^{*}(z)$ of the employed dye, and the local detection efficiency $Q(\vec{r})$. The spatial variation of $k(\vec{r})$ stems (i) from the local intensity of the excitation and the STED light and (ii) from the interaction of the emission dipole with the cover slip–sample interface in its proximity. The local variation of $q_{fl}^{*}(z)$ is caused by (ii) alone. For pulsed excitation and pulsed STED, $k(\vec{r})$ can be well described by $k(\vec{r}) \approx \left(1+\gamma(\vec{r})\exp\left(-k_{S1}^{*}(z)\tau_{STED}(1+\gamma(\vec{r}))\right)\right)/\left(1+\gamma(\vec{r})\right)$, where a rather long pulse width τ_{STED} of the STED pulse compared to that of the excitation pulse and a pulse period long compared to the excited state lifetime has been assumed [35]. The effective fluorescence suppression factor $\gamma(\vec{r}) = \zeta(\vec{r})k_{vib}/\left(\zeta(\vec{r})k_{S1}^{*}(z)+k_{vib}\right)$ depends on the vibrational relaxation rate k_{vib} within the electronic ground state, the spontaneous decay rate k_{S1} from the first excited state (inverse lifetime) and the fluorescence suppression factor $\zeta(\vec{r}) = I_{STED}(\vec{r})/I_s$ by STED, where I_s is the STED saturation intensity at which half of the spontaneous emission is suppressed [35]. The

#158306 - $15.00 USD Received 16 Nov 2011; revised 9 Feb 2012; accepted 10 Feb 2012; published 17 Feb 2012

proximity of the cover slip interface causes an additional dependence on the axial z-position, because the emission rate of the fluorophore increases [36,37]. The spontaneous decay rate k_{S1} of the excited state is increased by the average enhancement $\gamma_{fl}(z) \approx \left(2\gamma_{//}(z) + \gamma_{\perp}(z)\right)/3$ of radiative decays [33]. That is, when moving closer to the cover glass surface (z = 0), k_{S1} increases to $k^*_{S1}(z) = k_{S1}\left(1 - q_{fl} + q_{fl}\gamma_{fl}(z)\right)$, where q_{fl} is the normal fluorescence quantum yield (far away from the surface) and $\gamma_{//}(z)$ and $\gamma_{\perp}(z)$ are the enhancement factors for emission dipoles oriented parallel and perpendicular to the cover slip–sample interface, respectively [33,36]. The distance dependent fluorescence quantum yield thus accounts to $q^*_{fl}(z) = q_{fl}\gamma_{fl}(z)/(1 - q_{fl} + q_{fl}\gamma_{fl}(z))$. Furthermore, the x- and y-polarized components of the STED intensity (parallel to the interface) have to be weighted by $\left(1 - q_{fl} + q_{fl}\gamma_{fl}(z)\right)/\left(1 - q_{fl} + q_{fl}\gamma_{//}(z)\right)$ and the z–polarized component (perpendicular to the interface) by $\left(1 - q_{fl} + q_{fl}\gamma_{fl}(z)\right)/\left(1 - q_{fl} + q_{fl}\gamma_{\perp}(z)\right)$ in order to account for the polarization dependent modification of the STED action, i.e. of the efficiency of stimulated emission [35].

For the calculation of the final brightness profile $B(\vec{r})$, we thus need the fluorescence quantum yield q^*_{fl} (or q_{fl}) and the spontaneous decay rate k^*_{S1} (or k_{S1}), which should match our experimental conditions as closely as possible. In our TIRF-STED experiments, we used for example the fluorophore Atto647 (NHS-ester, Atto-Tec, Siegen, Germany) in PBS buffer solution or an Atto647N (Atto-Tec) labeled lipid analog (Atto647N–DOPE, *1,2-dioleyl-sn-glycero-3-phosphoethanolamine*, Atto-Tec, labeled at the head-group [12]) in supported lipid bilayers (SLB) of DOPC (*1,2-dioleoyl-sn-glycero-3-phosphocholine*, Avanti Polar Lipids, Alabaster, AL).

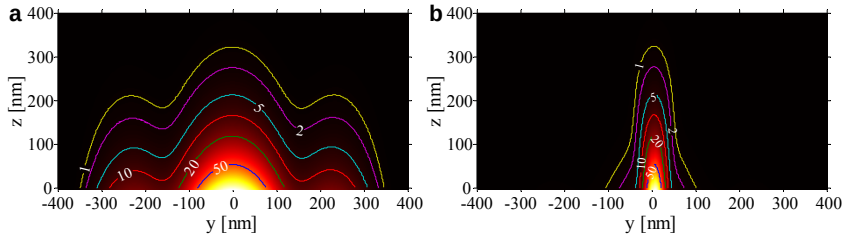

Fig. 5: Calculated normalized brightness profiles of the detected fluorescence emitted by Atto647 fluorophores dissolved in PBS buffer, (a) without STED and (b) with STED, respectively: lateral cross-section along the y-axis and contour lines along the axial z-penetration. The contour lines show the relative brightness in percent of the peak brightness at the focal center. The cover glass surface is at z = 0. (b) The STED beam had a pulse width τ_{STED} = 110 ps at a pulse rate of 79.3 MHz and a power to stimulate the emission 500× faster than spontaneous decay at the crest of the donut. A STED pulse delay of τ_{Δ} = 30 ps and a vibrational relaxation rate k_{vib} = 5/ps of Atto647 were assumed in this calculation.

For the NHS-ester of Atto647 in PBS buffer, we measured k_{S1} = (1.1 ns)$^{-1}$, which we used for the calculation of the brightness profile. Note that this value deviates from the vendor specification of k_{S1} = (2.3 ns)$^{-1}$ (Atto647–COOH in water, Atto-Tec). We used q_{fl} = 20% as specified because there is little influence on the brightness profile at low values. For Atto647N–DOPE, we measured k^*_{S1} ≈ (3.84 ns)$^{-1}$ in the DOPC SLB. We estimated the quantum yield q^*_{fl} in the SLB from values of q_{fl} = 65% and k_{S1} = (3.4 ns)$^{-1}$ specified for the pure dye Atto647N in PBS buffer (Atto-Tec). Assuming that the radiative decay rate k_{fl} is only influenced by the proximity of the cover slip but not by the lipophilic SLB environment, i.e. $k^*_{fl} = \gamma_{fl}k_{fl} \approx 1.17k_{fl}$ [36,37], and that, vice-versa, the non-radiative decay rate $k_{nr} = k_{S1} - k_{fl}$ is only sensitive to the environment, i.e. to the rate of collisions and the polarity of collision partners, we estimated $k^*_{nr} = k^*_{S1} - \gamma_{fl}k_{fl} \approx (3.84\ \text{ns})^{-1} - 1.17k_{fl}$, where $k_{fl} = 0.65(3.4\ \text{ns})^{-1}$. Hence,

#158306 - $15.00 USD Received 16 Nov 2011; revised 9 Feb 2012; accepted 10 Feb 2012; published 17 Feb 2012

far from the cover slip interface, the spontaneous decay rate of the Atto647N lipid analog in a lipid bilayer is estimated as $k_{S1} = k_{fl} + k_{nr}^{*} \approx (4.4\,\mathrm{ns})^{-1}$ and the fluorescence yield would be $q_{fl} \approx 84\%$, which correspond well to values measured in black lipid bilayers far away from the glass surface [38].

Figure 5 shows the calculated three-dimensional brightness profile when detecting the emission of Atto647 fluorophores dissolved in PBS buffer. Without STED (Fig. 5a), the FWHM diameter is ~160 nm (50% contour line), but much signal stems from the region of the first side lobe with ~450 nm diameter. With a STED beam driving the stimulated emission at a 500-fold increased rate (compared to the spontaneous decay) at the crest of the donut (Fig. 5b), only the central peak remains and its FWHM diameter shrinks to ~35 nm. The axial FWHM is ~55 nm in both cases. Due to the confocal detection and the enhanced fluorescence emission rate near the cover slip–sample interface, it is smaller than the penetration depth of 72 nm of the excitation light. It stays constant for different STED powers because it is exclusively determined by the evanescent character of the epi-TIRF modality and completely independent of the STED beam.

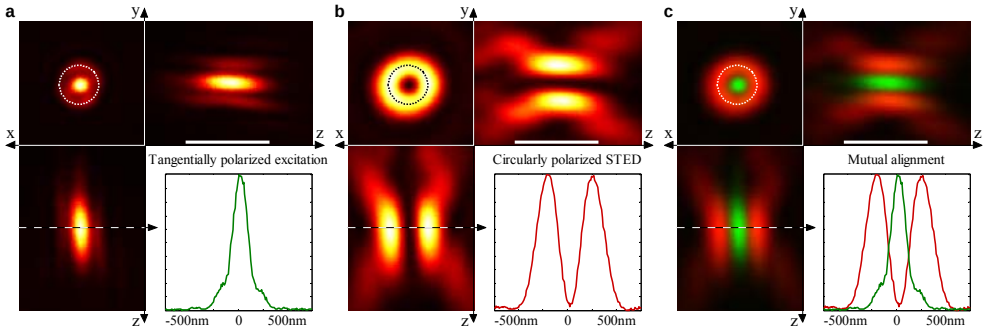

Fig. 6: Experimental profiles of (a) the excitation intensity × detection efficiency $I_{ex}{\cdot}Q$, (b) the STED intensity I_{STED} and (c) their overlap measured with a ∅80 nm gold bead immobilized on the cover slip surface. The PSFs were measured simultaneously by recording (a) the luminescence of the gold bead on the confocal fluorescence detector and (b) the back-scattered light on a non-confocal detector (PMT). (c) The dotted circle illustrates the projected confocal pinhole. The gold bead was mounted in immersion oil to minimize back-reflections of the laser light. Consequently, no evanescent field is created for the excitation due to the mounting in oil, but only the alignment and quality of the excitation PSF are probed. Scale bars: 1 µm.

3. Experiments and results

3.1 Experimental excitation and STED foci

The excitation and STED foci were aligned with the detection pinhole by maximizing the detected fluorescence of a micromolar Atto647 solution. This initial alignment was then refined by recording the focal light intensity distributions using a gold bead of 80 nm diameter (80 nm gold colloid, BBInternational, Cardiff, UK) immobilized with *Poly-L-Lysine* solution (0.1% w/v in water with 0.01% *Thimerosal*, Sigma-Aldrich, Steinheim, Germany) on the cover glass surface. Point spread function (PSF) cross-sections were recorded by scanning the gold bead through the foci. The confocal PSF of the excitation intensity times the detection efficiency was recorded by the luminescence of the gold bead (660–720 nm) detected on the confocal fluorescence detector, whereas the STED intensity was obtained simultaneously by the back-scattered STED light recorded on a non-confocal photo-multiplier tube (PMT). Figure 6 exemplifies such PSF scans for well-aligned foci. The gold bead was mounted in immersion oil to minimize the back-reflection of the laser light at the interface. Therefore, the axial cross-sections do not show the evanescent character of the TIRF focus above the cover slip but only the alignment and quality of the excitation PSF. Except for small deviations caused by aberrations, the measured PSFs agree with the calculations.

#158306 - $15.00 USD Received 16 Nov 2011; revised 9 Feb 2012; accepted 10 Feb 2012; published 17 Feb 2012

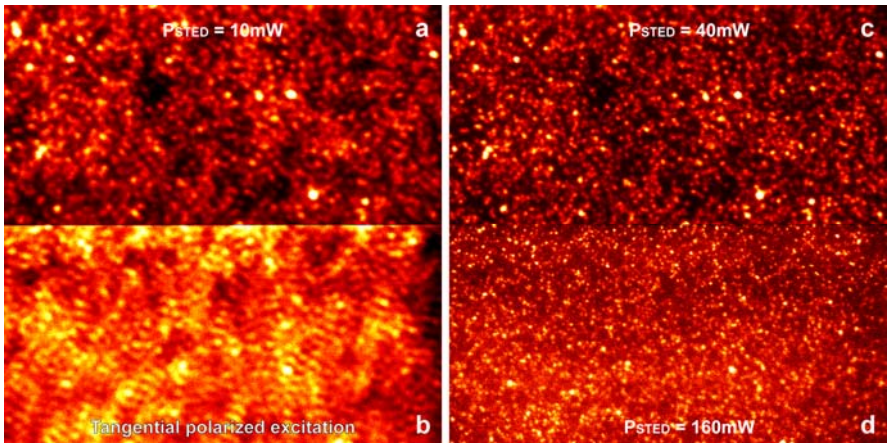

Fig. 7: Scanning images (normalized brightness) of ∅20 nm fluorescent beads immobilized on the cover slip for different STED powers of (a) 10 mW, (b) 2 mW, (c) 40 mW and (d) 160 mW following TIRF excitation with tangential polarization and donut shaped STED beam with circular polarization. Area: 10×10 μm^2, scanning step size 10 nm and dwell time 100 μs. (a), (c), (b) and (d) show the same sample areas.

3.2 Confocal epi-TIRF-STED nanoscopy

We imaged fluorescent beads of 20 nm diameter (crimson fluorescent FluoSpheres 0.02 μm, Invitrogen/Molecular Probes, Eugene, OR), which we randomly deposited on the cover slip. The beads were immobilized by *Poly-L-Lysine* solution and then immersed in pure water. Figure 7 exemplifies a few bead images obtained with the evanescent excitation PSF outlined in Fig. 2b (tangential polarization), the donut-like STED PSF outlined in Fig. 3a (circular polarization) and their overlay as outlined in Fig. 6. Recordings at low STED power (a) or with confocal TIRF without STED light do not resolve the beads, because the strong first side lobe creates ghost images (artifacts in Fig. 7b). At moderate STED power of 10 mW (a) and 40 mW (c), images with a reasonable contrast and well-suppressed side lobes were obtained. The measured FWHM diameter of the beads and thus the resolution of our microscope were improved from diffraction-limited (170–250) nm (we could not determine the FWHM better because of the poor contrast) to ~150 nm and 90 nm, respectively. At even higher STED powers, e.g. 160 mW (d), the FWHM diameter improved to ~60 nm. Accounting for the 20 nm diameter of the fluorescent spheres, we can estimate a lateral spatial resolution of ~55 nm FWHM of our microscope. Together with the calculated axial FWHM of ~55 nm, we obtained an almost isotropic sampling volume, approximately 250× smaller than that of an inherently diffraction-limited confocal microscope. Two issues prevented us from further increasing the STED power and thus further improving the lateral resolution. First, the SBR and thus the contrast of the images decreased for very small sampling volumes. Second, due to the TIRF illumination, the image quality is severely affected by a small defocus. For example, a defocus of (100–200) nm at the bottom of (d) due to a slightly tilted sample stage along the *y*-axis was sufficient to neutralize the improvement in resolution as compared to (c), even though a similar defocus was present in the upper part of (c). We attribute this decreased contrast and increased defocus sensitivity to an increased detection of fluorescence emitted in the outer side lobes of the excitation PSF, where the STED light is weak and cannot suppress the fluorescence sufficiently. It may also result from slight suppressions of fluorescence in the focal center (non-zero intensity at the center of the STED focus, c.f. [35]). Such filling up of the zero of the donut at high STED power may partially stem from the spectral broadening of the STED pulse. Because we had to circularize the polarization in front of the dichroic mirror, we were particularly sensitive to such spectral fluctuations introducing some ellipticity in the polarization of the STED beam. Our calculations show that besides high order aberrations like

#158306 - $15.00 USD Received 16 Nov 2011; revised 9 Feb 2012; accepted 10 Feb 2012; published 17 Feb 2012

coma, such non-circular polarizations are the major causes of an imperfect central ‘zero’ of the engineered STED focal intensity.

3.2.1. Polarization of the evanescent excitation

We measured the resolution achieved at 160 mW STED power when changing the polarization of the excitation beam (Fig. 8) and compared it with that achieved with the tangential polarization (Fig. 7d). For radial polarization (compare Fig. 2a), the FWHM diameter of the imaged beads was ~90 nm at 160 mW STED power (Fig. 8a). At 160 mW STED power, linear polarization led to ~85 nm (average along *x* and *y*, Fig. 8b) and circular polarization to ~70 nm (Fig. 8c) FWHM diameter, respectively. Consequently, tangential polarization as in Fig. 7 led to the best resolution of ~55 nm, because it only marginally excited fluorophores with *z*-oriented dipoles (compare Fig. 2b). As outlined in Fig. 3a, the emission of such fluorophores is hardly suppressed because the STED beam intensity has virtually no *z*-component at and in the closest vicinity of the central minimum. Because radial and linear polarization lead to excitation intensities with prevailing *z*-component, the emission of non-rotating or slowly rotating fluorophores is difficult to suppress, which explains why the lateral resolution was significantly improved in case of excitation with circular polarization (prevailing *x*- and *y*-intensity components in the focus) and, in particular, in case of tangential polarization yielding no *z*-intensity component at all (Fig. 2b).

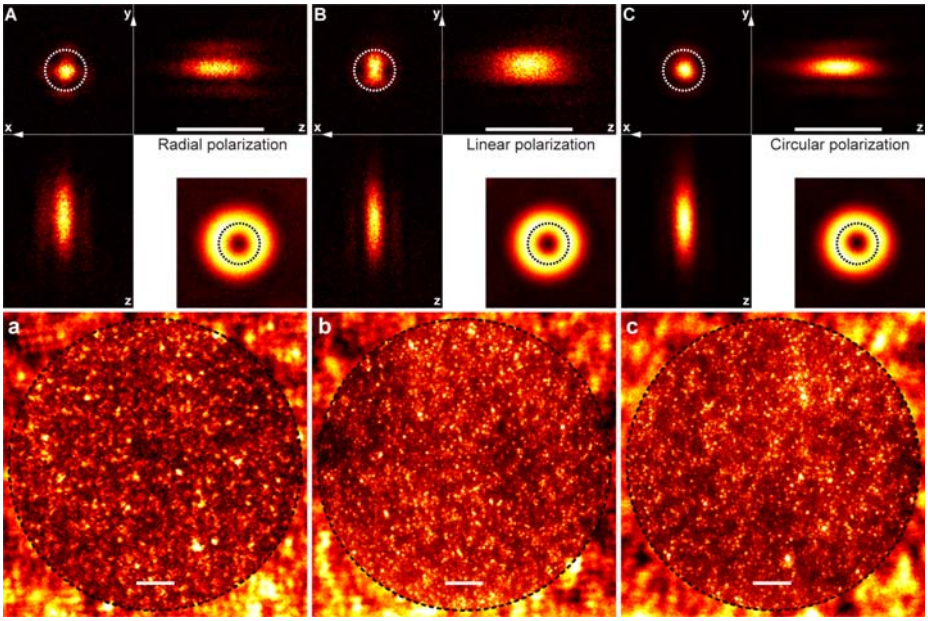

Fig. 8: Measured laser intensity profiles (A-C) and resulting TIRF-STED images (normalized brightness) of ∅20 nm fluorescent beads immobilized on the cover slip (a-c). The excitation light was polarized (A,a) radially, (B,b) linearly along the *y*-axis and (C,c) circularly, respectively. (A-C) The upper and left panels show the experimentally determined *xy*, *xz* and *yz* cross-sections of the excitation × detection profiles (as for Fig. 6 no evanescent field is created due to the mounting in oil), and the lower right panels the lateral *xy* cross-sections of the STED intensity profile. The circles indicate the size of the confocal pinhole as in Fig. 6. The images (a-c) show the diffraction limited performance in the outer parts and the TIRF-STED performance in the centers (STED power of 160 mW). Scale bars: 1 μm.

In all cases, the diffraction-limited confocal evanescent images without STED were more blurred than their non-evanescent counterparts (compare [34,30]) due to an evanescent excitation spot with much stronger side lobes (c.f. tangential polarization) and/or larger FWHM diameters with strong pedestals (c.f. radial polarization).

#158306 - $15.00 USD Received 16 Nov 2011; revised 9 Feb 2012; accepted 10 Feb 2012; published 17 Feb 2012

3.3 TIRF-STED-FCS

We carried out FCS experiments to further characterize the performance of the TIRF-STED nanoscope by monitoring the intensity fluctuations due to fluorophores diffusing in and out of the observation volume. As outlined before, we performed these measurements on two samples: (i) 0.2–0.5 μM solutions of Atto647 in PBS buffer (pH ≈ 7.4), and (ii) Supported-Lipid-Bilayers (SLBs) of DOPC containing a small fraction (≈ 10^{-4}) of the fluorescent lipid analog DOPE–Atto647N; see Chiantia et al. [39] for the SLB preparation protocol. Atto647 in PBS buffer served as sample exhibiting free three-dimensional diffusion, whereas the SLBs allowed free diffusion along the two lateral dimensions only, with the possibility to study the influence of background from freely diffusing fluorophores in the volume.

3.3.1 FCS fitting

Figure 9 shows a subset of auto-correlation curves $G_i(\tau)$ measured with DOPE–Atto647N freely diffusing in a DOPC SLB on a plasma-cleaned cover slip (a) and of Atto647 in PBS buffer (b). All $i = 1\ldots N$ curves of a measurement set were globally fitted using a set of calculated correlation curves $g(D\tau, P_{\mathrm{STED}} / P_{\mathrm{s}}, \tau_{\Delta})$ (see appendix) with the main fit model

$$G_i(\tau) = G_{\infty i} + \frac{g(D\tau, P_{\mathrm{STED}i} / P_{\mathrm{s}}, \tau_{\Delta})}{\langle C_i \rangle}\left(1 + \frac{p_{\mathrm{t}}}{1-p_{\mathrm{t}}}\exp\left(-\frac{\tau}{\tau_t}\right)\right) \qquad (1)$$

using the global fit parameters P_{s}, τ_{Δ}, D, p_{t} and τ_{t}, as well as fit parameters individual to each curve i such as the apparent average concentrations of fluorescent molecules $\langle C_i \rangle$ and the correlation offsets $G_{\infty i}$. D is the diffusion coefficient of the fluorescent molecules. p_{t} is the average fraction of excited molecules in the dark (triplet) state and τ_{t} the correlation time characterizing its population and depopulation kinetics [40]. P_{s} is the saturation power characterizing the molecule-specific efficiency of the STED light to inhibit spontaneous fluorescence emission (in the donut crest, 50% of the fluorescence emission is inhibited at the power P_{s} of the STED light), and $\tau_{\Delta} \approx 100$ ps is the delay between the excitation and the STED pulse. Using P_{s} and τ_{Δ} we can calculate for each STED power P_{STED} the brightness profile $B(\vec{r})$ and its effective FWHM diameter as outlined in Fig. 5. $P_{\mathrm{STED}}/P_{\mathrm{s}}$ and τ_{Δ} and thus $B(\vec{r})$ yield the auto-correlation template curves (5), $g(D\tau, P_{\mathrm{STED}} / P_{\mathrm{s}}, \tau_{\Delta})$, which define the shape and mutual relation of the curves $G_i(\tau)$, while $\langle C_i \rangle$ inversely scales their amplitudes.

We estimated the initial values of the parameters by fitting each individual correlation curve $G_i(\tau)$ using the model function (2) for anomalous diffusion through a two-dimensional Gaussian area.

$$G_i(\tau) = G_{\infty i} + \frac{G_{\mathrm{d}i}}{1 + (\tau / \tau_{\mathrm{d}i})^{\alpha_i}}\left(1 + \frac{p_{\mathrm{t}i}}{1-p_{\mathrm{t}i}}\exp\left(-\frac{\tau}{\tau_{\mathrm{t}i}}\right)\right) \qquad (2)$$

Here, we introduced the average transit time $\tau_{\mathrm{d}i}$ through the observation area and the anomaly coefficient α_i. Values of $\tau_{\mathrm{d}i}$ scale with the diameter of the sampling area and the diffusion coefficient D, while α_i quantifies deviations from normal free diffusion. α_i is 1 for normal and < 1 for anomalous diffusion, e.g., due to hindered diffusion from obstacles in the diffusion pathway. For the global fit (1), the values of $G_{\infty i}$ were fixed individually at the so-estimated values. The triplet parameters were fixed for all curves to the averages of the $i = 1\ldots N$ estimated values of $p_{\mathrm{t}i}$ and $\tau_{\mathrm{t}i}$. The values of $\tau_{\mathrm{d}i}$ allowed estimating the start values of D and P_{s} by matching the observed decrease of $\tau_{\mathrm{d}i}(P_{\mathrm{STED}})$ with the calculated relation in function of $P_{\mathrm{STED}} / P_{\mathrm{s}}$. Finally, the initial values of $\langle C_i \rangle$ were obtained from the correlation amplitudes $G_{\mathrm{d}i} = g(0, P_{\mathrm{STED}i} / P_{\mathrm{s}}, \tau_{\Delta}) / \langle C_i \rangle$. The model function (2) is also sufficient for the estimation of

#158306 - $15.00 USD Received 16 Nov 2011; revised 9 Feb 2012; accepted 10 Feb 2012; published 17 Feb 2012

the initial parameters of the correlation data recorded for free Brownian diffusion in a three-dimensional volume, in which case α_i simply tends to be ≈ 1.

3.3.2 FCS experiments

Figure 9 shows FCS data of the fluorophore Atto647 in PBS buffer (pH ≈ 7.4) and of the fluorescent lipid analog DOPE–Atto647N diffusing in SLB membranes. As expected, the auto-correlation curves shift to shorter correlation lag times for increasing STED powers P_{STED}, since the diffusion through the smaller observation spots takes less time [12–14]. As Fig. 9 shows, all curves of a set can be well described by our global fit model (1).

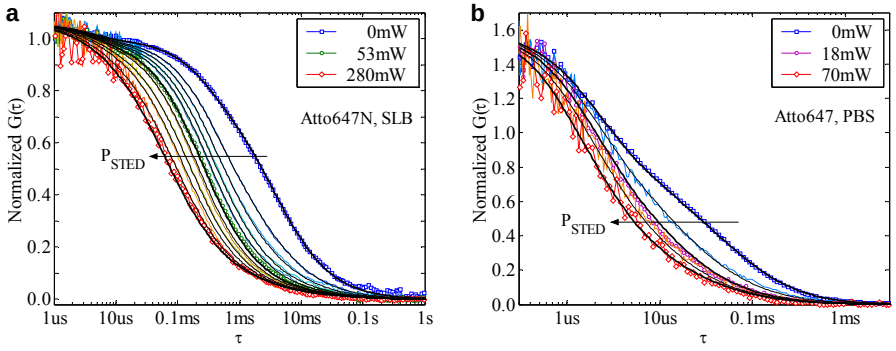

Fig. 9: TIRF-STED-FCS. Normalized measured (colored markers) and fitted (black lines) auto-correlation curves for (a) DOPE–Atto647N diffusing in a DOPC SLB measured with STED powers P_{STED} in the sample of {0, 11, 18, 26, 35, 53, 70, 105, 140, 210, 280} mW and (b) a 0.5 µM solution of Atto647 in PBS buffer measured with P_{STED} = {0, 7, 18, 35, 70} mW. The FCS measurements lasted 30s each. The extracted fit parameters are: (a) D ≈ 5.0 µm^2/s, P_s ≈ 8.8 mW, and FWHM ≈ {157, 80, 39} nm at P_{STED} = {0, 53, 280} mW, respectively, and (b) D ≈ 156 um^2/s, P_s ≈ 2.7 mW, FWHM ≈ {156, 91, 53} nm at P_{STED} = {0, 18, 70} mW, respectively.

We determined P_s ≈ 8.8 mW and ≈ 2.7 mW for Atto647N–DOPE in SLB and Atto647 in PBS, respectively, which resulted in observation spots of diameters down to FWHM ≈ 39 nm for Atto647N–DOPE in SLB (P_{STED} = 280 mW) and down to FWHM ≈ 50 nm for Atto647 in PBS (P_{STED} = 70 mW). The extracted diffusion coefficient D ≈ 5 µm^2/s in the SLB coincides well with previous measurements on similar model membranes [41,42]. We found a small triplet population p_t ≈ 6% with a correlation time τ_t ≈ 4 µs. In the aqueous environment, we measured D ≈ 160 µm^2/s for Atto647, which is comparable to the diffusion coefficient of other small organic fluorophores [43]. Atto647 showed a significant triplet population of p_t ≈ 39% with a correlation time τ_t ≈ 2.2 µs. These triplet parameters were extracted from the auto-correlation curve measured without STED because the triplet kinetics and the diffusion became nearly indistinguishable with STED. The anomaly factor α_i was ≈ 0.8–1 in the SLB measurements and ≈ 1 in PBS.

3.3.3 Signal-to-background ratio

The signal-to-background ratio (SBR) of the experiment determines the quality and noise of the correlation data and therefore the accuracy to determine parameters from the curve fitting. The background may result from scattering or fluorescence induced by the STED light, from the ambient light, from the detector dark current, from reflected excitation light, and most importantly, from fluorescence contributions from the outer side lobes of the evanescent excitation modality. Even if the background signal stays constant for increasing STED power (such as for the contributions from the outer side lobes), the SBR would degrade because the signal decreases with the sampling volume. Consequently, at high STED powers, the increased contribution of background signal from the non-suppressed fluorescence of the second and outer side lobes (compare also Fig. 7) resulted in a reduction of the SBR and thus

#158306 - $15.00 USD Received 16 Nov 2011; revised 9 Feb 2012; accepted 10 Feb 2012; published 17 Feb 2012

in enhanced noise in the measured auto-correlation curves, a damping of the correlation amplitude $G_{di} \sim 1/\langle C_i \rangle$, and consequently in increased values of $\langle C_i \rangle$ [44]. This degradation of the SBR did not allow us to apply STED powers larger than 280 mW in SLBs and 70 mW for Atto647 in PBS buffer for achieving reliable correlation curves, i.e. to realize observation areas significantly smaller in diameter than ≈ 40 nm and ≈ 55 nm, respectively. In principle, one may correct for this damping effect by introducing the factor $SBR^2(1 + SBR)^{-2}$ [44], but the required knowledge of SBR values is in general not easy to assess accurately. In the given example of DOPE–Atto647N diffusion in the SLB, the apparent surface density $\langle C_i \rangle$ was (80–90)/μm^2 at low STED power and ~120/μm^2 at 280 mW, where our fit model took into account most of the background contribution from the outer side lobes. The background caused by the STED light, the ambient light and the detector dark current contributed to the remaining variation of the apparent surface density.

3.3.4 Molecular brightness

The average count rate per molecule (CPM) calculated from the product of G_{di} and the total signal [44,14] was 120–150 kHz for DOPE–Atto647N in the SLB and 80–110 kHz for Atto647 in PBS buffer with our pulsed excitation and a moderate average excitation power of 30–100 μW, i.e. 20–60 kW/cm^2. The CPM values were about twice the brightness obtained with water immersion objectives and non-evanescent excitation. Taking the brightness profile into account, the peak count rate in the center of the observation volume was estimated to be ~500–600 kHz per molecule.

3.3.5 Comparison of Atto647 and Atto647N-lipid data

In our TIRF-STED-FCS experiments on Atto647N-labeled lipids and Atto647 in solution, we achieved a confinement of the observation area of down to 40 nm and ~55 nm FWHM, respectively. The slightly worse performance of TIRF-STED-FCS for Atto647 results from several factors. Most importantly, the fluorescence quantum yield of Atto647 (q_{fl} = 20%) is much lower than that of Atto647N in SLB (q_{fl} ≈ 84%), resulting in lower CPM values and deteriorating the quality of correlation experiments in general [44]. Therefore, we could not measure reliable Atto647 correlation data in sampling spots as small as for Atto647N. Further, the lifetime of Atto647 is much shorter, ≈ 1 ns near the cover slip interface compared to ≈ 4ns for Atto647N in SLB. Consequently, for the Atto647 measurements, the delay of the STED pulse with respect to the excitation pulse was shortened, which in principle improves the STED efficiency and thus the achievable FWHM resolution [35]. However, it also introduced minor artifacts in the correlation data (oscillations at $\tau < 1$ μs, spikes for $\tau > 3$ ms) due to jitter in the pulse timing. Also, as the free Atto647 dye diffused fast, the transit time τ_d became comparable to the triplet correlation time $\tau_t \approx 1.3$ μs at high STED powers, making analysis of the curves more difficult [14]. Despite the shorter lifetime, the saturation power $P_s \approx 3$ mW of Atto647 in PBS is about three times smaller than for the Atto647N sample ($P_s \approx 9$ mW), which at the same P_{STED} allows obtaining a better resolution for Atto647 compared to Atto647N in SLB (e.g. 53 nm compared to 71 nm FWHM at P_{STED} = 70 mW, respectively). The lower saturation power may be attributed to a several times larger STED cross-section of Atto647 (broader emission spectrum) and a higher rotational mobility of the dye in the PBS buffer (reduced orientation effects) as compared to the Atto647N dye in the SLB [45].

3.4 Comparison of STED-FCS and TIRF-STED-FCS

Previous confocal STED-FCS measurements on samples with fluorophores diffusing in three dimensions outlined a strong deterioration of the SBR at large STED powers due to an increased contribution of out-of-focus signal (i.e. increased contributions of uncorrelated fluorescence signal from above or below the observation volume) [13,14]. This issue could be well eluded by measuring on two-dimensional samples such as membranes, delivering excellent SBRs down to 30 nm small sampling spots, able to give new insights into important

#158306 - $15.00 USD Received 16 Nov 2011; revised 9 Feb 2012; accepted 10 Feb 2012; published 17 Feb 2012

biological questions such as the heterogeneous dynamics and organization of lipids in the plasma membrane of living cells [12,14]. While confocal STED-FCS measurements of freely diffusing fluorophores in open, three-dimensional detection volumes were in general possible down to sampling spot diameters of 50–70 nm, the correlation amplitudes G_d were, due to the increased contribution of out-of-focus signal, damped by up to a factor of 1.5 in aqueous environment instead of increasing by a factor of 10 as measured by the 10-fold decrease of the transit time τ_d [14]. Along with the 6-fold decrease of τ_d (from 25 µs without STED to 4 µs for a STED power of 70 mW) our TIRF-STED-FCS measurements of Atto647 in solution showed a 3-fold increase of G_d, i.e. a much lower damping of the amplitude G_d and thus much lower deterioration of the SBR. While we have to tackle an increased contribution of signal from the second and outer side lobes in our TIRF-STED-FCS measurements, out-of-focus signal seems to be only a minor issue unlike in the confocal STED-FCS experiments. Therefore, the question arises how both nanoscopy FCS techniques perform on membranes with an increased out-of-focus background contribution such as from inner-cellular (auto) fluorescence, e.g., live cells quickly internalizing fluorescent constituents from the membrane.

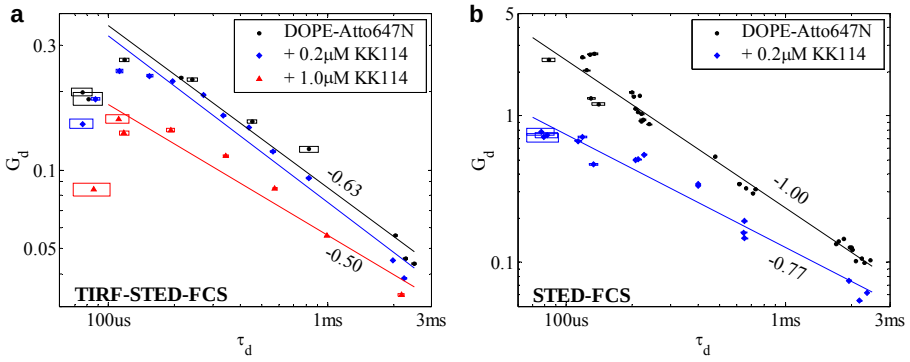

Fig. 10: STED-FCS in the presence of out-of-focus background. Correlation amplitudes G_d versus transit times τ_d for various STED powers P_{STED} for (a) TIRF-STED-FCS and (b) confocal STED-FCS. All parameters were extracted using the fit model (2) for anomalous diffusion in two dimensions. Rectangles indicate the 95% confidence intervals of the fitted parameters (least squares fit). Thin lines show the (partial) linear regressions of $G_d(\tau_d)$. Ideally, a linear correlation between $\log(G_d)$ and $\log(\tau_d)$ with a slope of –1 is expected. A shallower slope indicates a reduction of the SBR with increasing STED power.

For comparing the performance of our instrument on membranes exhibiting significant out-of-focus background with that of a typical confocal nanoscope equipped with a 1.40 NA oil immersion objective, we performed STED-FCS measurements of the same DOPC SLB containing DOPE–Atto647N on both instruments. For testing the background rejection, we added some freely diffusing fluorophore KK114 [46] to the buffer solution. We used the hydrophilic fluorophore KK114 because it showed nearly no transient binding to the SLB. We repeated the STED-FCS measurements on both instruments with a concentration of ~0.2 µM and 1 µM KK114. Figure 10 summarizes the results by showing the correlation amplitudes G_d versus the transit times τ_d, which were both extracted from the individual FCS curves recorded with increasing STED power of (0–280) mW using the fit model (2) for two-dimensional anomalous diffusion. Values of G_d increase and those of τ_d decrease with increasing STED power and thus decreasing observation spot diameter, as expected [14]. However, G_d is inversely proportional to the average number of particles in the observation volume *and* proportional to the factor $SBR^2(1 + SBR)^{-2}$ [44], which accounts for the background, whereas τ_d is simply proportional to the observation area. Ideally, $G_d \times \tau_d$ would be independent of the STED power, i.e. a linear correlation between $\log(G_d)$ and $\log(\tau_d)$ with a slope of –1 is expected for freely diffusing fluorophores. Photo-bleaching of fluorophores due to the STED

#158306 - $15.00 USD Received 16 Nov 2011; revised 9 Feb 2012; accepted 10 Feb 2012; published 17 Feb 2012

light would lead to a steeper slope (due to a reduction of τ_d [14]), whereas a shallower slope indicates a reduction of the SBR with increasing STED power (due to a damping of G_d).

Because KK114 diffuses about 30× faster and is approximately as bright as DOPE–Atto647N, it diminishes the observed transit time if its contribution becomes significant. As Fig. 10a clearly shows, our TIRF-STED instrument was able to measure the diffusion characteristics of DOPE–Atto647N alone at all conditions, because the transit times hardly changed when adding KK114. At 0.2 μM KK114, the correlation amplitudes were just reduced by ~20%, whereas at 1 μM they were reduced by (30–50)%. That is, the background from KK114 amounted only to ~10–30% of the total signal. For comparison, Fig. 10b shows the results obtained from the very same samples when measured on the confocal STED microscope. Without background, this microscope rendered excellent measurements with similar transit times but 2–5× larger correlation amplitudes for reasons discussed later. At 0.2 μM KK114, the diffusion characteristics of DOPE–Atto647N was well measured but the correlation amplitudes were already reduced by 40–70%, i.e. the KK114 background covered ~25–45% of the total signal. At 1 μM, the KK114 background was significantly stronger than the DOPE–Atto647N fluorescence. These STED-FCS measurements failed because we were unable to avoid detector saturation while keeping the SNR of the FCS measurements on an acceptable level for meaningful parameter extraction.

Our confocal TIRF-STED microscope proved to reject out-of-focus background fluorescence to a high degree, which renders it a candidate for STED-FCS measurements on layered structures in the presence of background fluorescence from the volume. However, it is worth noting that the confocal microscope performed significantly better than the TIRF setup when no or only little background was present. Without background, the slopes of the linear regressions in Fig. 10b are close to –1 for confocal STED-FCS, which indicates that the STED scaling of the observation area did not compromise the SBR of the measurement. Under this condition, the product $G_d \times \tau_d$ is invariant with P_{STED} because τ_d scales with the observation area and G_d with its inverse [14]. In addition, at low STED powers, confocal STED-FCS achieves smaller spots ($\tau_d \approx 0.6$ms compared to ~1ms) and 2–3× larger correlation amplitudes than TIRF-STED-FCS. This drawback of TIRF-STED-FCS obviously stems from the larger diffraction-limited spot of the evanescent illumination with its large side lobes (Fig. 2b). In principle, TIRF-STED should mostly compensate this penalty when powering the STED beam up (as shown for the images in Fig. 7a–c). However, the slopes of the linear regressions $G_d(\tau_d)$ (i.e. the parameter m in $\log(G_d) = m*\log(\tau_d) + b$) were shallower (slope of –0.63) and the measured correlation amplitudes remained significantly smaller than those obtained with the confocal microscope (Fig. 10a). We attribute this issue to a deterioration of the SBR with the STED power resulting from the increased influence of the second and higher side lobes (compare Fig. 7d), which became evident at the largest STED powers for which the correlation amplitudes declined instead of continuing to rise.

4. Conclusions

We showed how to achieve a three-dimensional confinement of the measurement volume to nanoscopic scales with commercial optics by combining confocal TIRF and STED. Confocal TIRF may be compared with a 4Pi microscope [47], which achieves a comparable axial confinement by two counter-propagating beams instead of internal reflection (see also Gu and Sheppard [48]). Compared to 4Pi microscopy, TIRF has the advantage of providing a monotonously decreasing excitation field without axial side lobes and, in epi-fluorescence configuration, of allowing simple experimental access to the sample, of course at the expense of having to work close to the cover glass surface. In our experiments, the confocal pinhole and STED confined the brightness profile laterally. Thanks to the high STED efficiency of the donut-shaped STED beam, the first side lobe of the TIR excitation was efficiently suppressed such that only spontaneous fluorescence from the center reached the detector. A comparison of different polarization modes revealed the most efficient STED action for tangentially polarized excitation light.

#158306 - $15.00 USD Received 16 Nov 2011; revised 9 Feb 2012; accepted 10 Feb 2012; published 17 Feb 2012

The TIRF-STED-FCS measurements on free three-dimensional diffusion of fluorophores in aqueous solution or on two-dimensional diffusion of fluorescent lipid analogs in SLBs not only matched our theoretical description, but also performed better with respect to fluorescence background from the volume than confocal STED-FCS. This reduction in fluorescence background allowed us to record accurate TIRF-STED-FCS data in observation volumes laterally confined down to ~50 nm in diameter. Together with a calculated axial confinement to ~55 nm due to the TIRF mode, we achieved an almost isotropic sampling volume of ~0.2 attoliter, approximately 250× smaller than a diffraction-limited confocal volume. Unfortunately, a further improvement of the lateral resolution was hampered by a loss in SBR. Furthermore, we qualified the performance of our epi-TIRF-STED nanoscope by imaging immobilized ∅20 nm fluorescent beads. We chose a dense concentration of beads, such that not only the resolution but also the contrast became evident. Lateral resolutions of ~70–100 nm in FWHM diameter were achieved at moderate STED powers. At resolutions better than ~60 nm the image contrast deteriorated, which lines up with the observed loss of SBR in the TIRF-STED-FCS recordings at high STED powers.

In summary, the performance of the outlined instrument regarding improved SBR suffers from limitations of the lateral instead of the axial contrast, which limits the useful lateral resolutions to ~50–100 nm in FWHM diameter for most samples. The reason for this lies in the strong side lobes of the confocal TIRF excitation modality and does not result from the STED implication. TIRF-STED nanoscopy and TIRF-STED-FCS can be a viable method for measurements at the cover slip surface, in particular if these measurements suffer from fluorescence background generated in the volume.

Appendix

A. Confocal epi-TIRF-STED nanoscope setup

Please refer to Fig. 1, which outlines the setup of our epi-TIRF-STED nanoscope. We used a high numerical aperture (NA) oil immersion objective (TIRFM UIS 2 Apo N 60× 1.49 NA oil, Olympus, Hamburg, Germany) featuring a correction ring for compensating the cover slip thickness and the dispersion of the immersion oil (Type F, Olympus). The objective was mounted vertically, such that the sample was freely accessible from above. A three-axis piezo stage (17PCZ013, Melles Griot, Bensheim, Germany) with differential micrometer screws allowed 4 mm manual travel with micrometer precision and 20 μm travel with nanometer precision for positioning the sample with respect to the objective. Image and PSF recordings were taken by piezo-driven stage/sample scanning.

A.1 Excitation

A pulsed picosecond laser (LDH-D-C-640 with PDL 800-D driver, PicoQuant, Berlin, Germany) provided laser pulses with $\tau_{ex} \approx 65$ ps pulse width at half-maximum at a wavelength $\lambda_{ex} \approx 640$ nm and a pulse rate of up to 80 MHz. The laser beam was coupled into a polarization maintaining single-mode fiber (PMC-630-4,6-NA011-3-XPC-200-P, Schäfter+ Kirchhoff, Hamburg, Germany) in order to clean up the mode profile. A 20× 0.35 NA objective (Leitz, Wetzlar, Germany) was used to collimate the excitation beam at the fiber output. A conical lens (linear axicon, 178° cone angle, Delmar Photonics, San Diego, CA) created the required ring illumination with ~8.6 mm diameter, which was then projected into the objective aperture (8.9 mm in diameter) by a Kepler telescope detuned to ~430 mm focal length. A Glan-Thompson polarizer (B. Halle, Berlin, Germany) rectified the linear polarization, before a polarization controller (radial polarization converter by ARCoptix, Neuchâtel, Switzerland) modified it either to tangential or to radial polarization. In case of tangential polarization, a 2π phase ramp (629 nm mask, vortex plate VPP-A, RPC Photonics, Rochester, NY) was inserted. A tunable half-wave plate (Alphalas, Göttingen, Germany) compensated the elliptical polarization introduced by the dichroic mirrors and the dielectric mirror in front of the objective. The sub-critical angle illumination was minimized by a

#158306 - $15.00 USD Received 16 Nov 2011; revised 9 Feb 2012; accepted 10 Feb 2012; published 17 Feb 2012

circular stop (chromium layer on glass substrate) blocking the central part of the excitation beam up to a diameter of 8.2 mm. A band pass filter (MaxDiode 640/8, AHF Analysentechnik, Tübingen, Germany) cleaned up the laser line and the dichroic mirror (Z647rdc, AHF) separated the emitted fluorescence from the excitation light.

A.2 Stimulated emission depletion

The STED power was generated by a mode-locked Ti:Sapphire laser system (MaiTai, Newport/Spectra-Physics, Darmstadt, Germany), which delivered femtosecond pulses at a pulse rate of 79.3 MHz and with an average power of 1.9 W at the wavelength λ_{STED} = 780 nm. A Faraday isolator (FI-780-5 SV, Linos Photonics, Göttingen, Germany) and a polarizing beam splitter cube prevented back-reflections into the laser cavity. A laser power controller (LPC-NIR, Brockton Electro-Optics, Brockton, MA) maintained a constant average STED power and allowed its adjusting. Home-made SF6 glass rods (3×18 cm) pre-stretched the laser pulses before the STED beam was coupled into a 100 m long polarization maintaining single-mode fiber (PMJ-A3HPC,3S-633-4/125-3-100-1-SP, AMS Technologies, Munich, Germany), in which the pulses dispersed to the final pulse width of $\tau_{STED} \approx 110$ ps. The STED beam was coupled out by an achromatic lens (doublet, 50 mm focal length) and a Glan-Thomson polarizer (B. Halle) rejected any residual orthogonal polarization. With a half-wave and a quarter-wave plate ($\lambda/2$, $\lambda/4$, (500–900) nm, B. Halle), the linear polarization was rendered elliptical such that it became circular in the objective aperture. A 2π phase ramp (796 nm mask, vortex plate VPP-A, RPC Photonics) induced the donut-shaped intensity profile on the STED beam. The STED beam was then enlarged to a $1/e^2$ beam waist of ~13 mm in diameter and projected by a dichroic mirror (Z770sprdc, AHF) and a dielectric mirror into the objective aperture.

A.3 Fluorescence detection

The emitted fluorescence was collected by the objective and transmitted through the dichroic mirrors. The tube lens (achromatic doublet, 400 mm focal length) projected it onto a gradient-index multimode 50:50 fiber splitter (Fiber Optic Network Technology Co, Surrey, BC, Canada) serving as pinhole with a diameter of 62.5 μm. With the chosen tube lens, the transversal magnification was effectively 133×, such that the projected pinhole diameter was ~470 nm in the sample space (0.85× the Airy disc diameter). Two band pass filters (HQ690/60m, AHF), ~20 cm distant in the converging beam, blocked the laser light, such that less than 10^{-12} of back-reflected and stray light was transmitted to the pinhole. Finally, two single-photon counting modules (SPCM-AQR-13-FC, PerkinElmer, Salem, MA) recorded the photons. Their signals were analyzed by (i) a hardware correlator (Flex02-01D/C, Correlator.com, Bridgewater, NJ) to calculate the auto-correlation of the intensity trace during FCS measurements, (ii) a multichannel analyzer/dual input multiscaler (MCA-3 Series/P7882, FAST ComTec, Oberhaching, Germany) for image recordings and PSF scans, and/or (iii) a picosecond lifetime and photon counter (DPC-230, Becker & Hickl, Berlin, Germany) for time-correlated single-photon counting (TCSPC) measurements and photon trace recordings with 82 ps time resolution.

A.4 Complementary detections

In front of the tube lens, a second Z770sprdc mirror (AHF) extracted a small fraction of back-reflected laser light that made it through the other dichroic mirrors. During alignment and PSF measurements, the back-reflected STED light was projected onto the active area (∅4 mm) of a photo-multiplier tube (MD-973, PerkinElmer). Simultaneously, the excitation and detection PSF were measured in the fluorescence channel by detecting the auto-luminescence of the gold beads. Finally, upon visual inspection and focusing, the back-reflected excitation light was imaged with another 400 mm tube lens into an eyepiece. A high pass filter prevented the STED light from reaching the eye.

#158306 - $15.00 USD Received 16 Nov 2011; revised 9 Feb 2012; accepted 10 Feb 2012; published 17 Feb 2012

A.5 Synchronization and timing

The pulsed laser diode was externally triggered via an electrical ps-delay box (in-house design and manufacture) by the synchronization output of the MaiTai Ti:Sapphire laser. The delay box allowed tuning the lag time between the excitation pulse and the STED pulse in steps of 2.5 ps. The synchronization output of the laser diode was used as clock signal for lifetime and TCSPC measurements.

B. Auto-correlation fit templates for FCS

Here, we summarize the calculation of the shape of the auto-correlation functions versus the STED power, which we used for global fitting of a set of FCS correlation curves obtained when measuring freely diffusing fluorophores in two or three dimensions. We concentrate on a few particularities as the calculation is well known and outlined in detail in the literature, see for example chapter 4 of the doctoral thesis by K. Hassler [49].

We start with the calculated brightness profile $B(\vec{r})$ of the detected fluorescence. If a fluorophore diffuses through this focus, the auto-correlation of the detected fluctuating intensity $I(t)$ writes as

$$G(\tau)=\frac{(T-\tau)\int_0^{T-\tau} I(t)I(T+\tau)\,\mathrm{d}t}{\left(\int_0^{T-\tau} I(t)\,\mathrm{d}t\right)\left(\int_\tau^{T} I(t)\,\mathrm{d}t\right)}=1+\frac{\iint B(\vec{r})B(\vec{r}')\phi(\vec{r},\vec{r}',\tau)\,\mathrm{d}\vec{r}\,\mathrm{d}\vec{r}'}{\left(\langle C\rangle\int B(\vec{r})\,\mathrm{d}\vec{r}\right)^2}, \qquad (3)$$

where T is the measurement time, τ the lag time, $\langle C\rangle$ the average concentration of fluorescing molecules and $\phi(\vec{r},\vec{r}',\tau)=\langle C\rangle(4\pi D\tau)^{-d/2}\exp\left(-(\vec{r}-\vec{r}')^2/(4D\tau)\right)$ is the probability that a fluorophore emits a photon at position $\vec{r}'$ after some time τ if it emitted one at position $\vec{r}$ before. D is the diffusion constant and d specifies the number of dimensions along which free diffusion takes place (1, 2 or 3). Let $\vec{\rho}$ be the lag distance such that $\vec{r}'=\vec{\rho}+\vec{r}$. Thereby, we can separate the dual-integral in the numerator of Eq. (3) and write

$$G(\tau)=1+\frac{(4\pi D\tau)^{-d/2}}{\langle C\rangle}\frac{\int\exp\left(-\rho^2/(4D\tau)\right)\int B(\vec{r})B(\vec{r}+\vec{\rho})\,\mathrm{d}\vec{r}\,\mathrm{d}\vec{\rho}}{\left(\int B(\vec{r})\,\mathrm{d}\vec{r}\right)^2}. \qquad (4)$$

The inner spatial integral can be evaluated using fast Fourier transforms and the convolution theorem, i.e. $\int B(\vec{r})B(\vec{r}+\vec{\rho})\,\mathrm{d}\vec{r}=B(\vec{r})\otimes_{\vec{r}}B(-\vec{r})$. The outer spatial integral can be performed as a line integral because the exponent only depends on the length ρ of the lag distance. Hence, we define $W(\rho)=\int_0^{\pi}\rho\cos\theta\int_{-\pi}^{+\pi}\rho\left(B\otimes_{\vec{r}}B\right)(\rho\sin\theta\cos\varphi,\rho\sin\theta\sin\varphi,\rho\cos\theta)\,\mathrm{d}\varphi\,\mathrm{d}\theta$ and get, exempt of the constant offset term and the concentration, the auto-correlation template

$$g(D\tau)=(4\pi D\tau)^{-d/2}\left(\int B(\vec{r})\,\mathrm{d}\vec{r}\right)^{-2}\int\exp\left(-\rho^2/(4D\tau)\right)W(\rho)\,\mathrm{d}\rho\,. \qquad (5)$$

The complete FCS auto-correlation model function writes then as

$$G(\tau)=G_\infty+G_d(\tau)G_t(\tau)=G_\infty+\frac{g(D\tau)}{\langle C\rangle}\left(1+\frac{p_t}{1-p_t}\exp\left(-\frac{\tau}{\tau_t}\right)\right), \qquad (6)$$

#158306 - $15.00 USD Received 16 Nov 2011; revised 9 Feb 2012; accepted 10 Feb 2012; published 17 Feb 2012

where G_∞ is the fitted offset, G_d is the diffusion term, and G_t is a kinetic term, which accounts for example for the triplet kinetics of the fluorophore. p_t is the fraction of fluorophores in the triplet state and τ_t is the triplet correlation time. The main global fit parameters are the diffusion constant D and the fluorophore concentration $\langle C \rangle$. Because the STED powers are known, the saturation power P_s can be extracted as well, which is tantamount to estimating the rate of stimulated emissions k_{STED} in the crest along with the effective brightness profile $B(\vec{r})$ and its FWHM diameter for the given STED powers. It is also possible to estimate the delay τ_Δ between the excitation and the STED pulse. P_s and τ_Δ are extracted by best matching the shapes and mutual relations of the experimental correlation curves with the calculated curves $g(D\tau, k_{STED}, \tau_\Delta)$, which are simply interpolated from a small set of predetermined templates.

Acknowledgments

We thank Dr. Iwan Märki, École Polytéchnique Fédérale de Lausanne (EPFL), Switzerland, for critical and helpful discussions. Marcel Leutenegger is a fellow of the Alexander von Humboldt foundation, Germany. Andreas Schönle provided the imaging software Imspector.

#158306 - $15.00 USD Received 16 Nov 2011; revised 9 Feb 2012; accepted 10 Feb 2012; published 17 Feb 2012